GEOPHYSICS, VOL. 72, NO. 6 (NOVEMBER-DECEMBER 2007); P. T67–T79, 16 FIGS., 1 TABLE.
10.1190/1.2785978

Rayleigh-to-shear wave conversion at the tunnel face — From 3D-FD modeling to ahead-of-drill exploration

Thomas Bohlen[1], Ulrich Lorang[2], Wolfgang Rabbel[2], Christof Müller[2], Rüdiger Giese[3], Stefan Lüth[3], and Stefan Jetschny[1]

ABSTRACT

For safe tunnel excavation, it is important to predict lithologic and structural heterogeneities ahead of construction. Conventional tunnel seismic prediction systems utilize body waves (P- and S-waves) that are directly generated at the tunnel walls or near the cutter head of the tunnel boring machine (TBM). We propose a new prediction strategy that has been discovered by 3D elastic finite-difference (FD) modeling: Rayleigh waves arriving at the front face of the tunnel are converted into high-amplitude S-waves propagating further ahead. Reflected or backscattered S-waves are converted back into Rayleigh waves which can be recorded along the sidewalls. We name these waves RSSR waves. In our approach, the front face acts as an S-wave transceiver. One technical advantage is that both the sources and the receivers may be placed behind the cutter head of the TBM. The modeling reveals that the RSSR waves exhibit significantly higher amplitudes than the directly reflected body waves. The excavation damage zone causes dispersion of the RSSR wave leading to multimodal reflection response. For the detection of geologic interfaces ahead, RSSR waves recorded along the sidewalls are corrected for dispersion and stacked. From the arrival times, the distance to the S-S reflection point can be estimated. A recurrent application, while the tunnel approaches the interface, allows one to quantify the orientation of the reflecting interfaces as well. Our approach has been verified successfully in a field experiment at the Piora adit of the Gotthard base tunnel. The distance to the Piora fault zone estimated from stacked RSSR events agrees well with the information obtained by geologic surveying and exploratory drilling.

INTRODUCTION

Underground construction is often carried out under complex soil and rock conditions. An important factor in tunnel excavation is the knowledge of the geologic environment and the geotechnical parameters to be encountered. Unrecognized and unexpected decreases in rock quality or fluid inflows represent a danger for humans and machines. It is therefore of great importance to develop techniques that can localize geologic heterogeneities, such as caverns, faults, erratic rocks, fracture zones, and wet layers (aquifers) before tunnel construction reaches such areas. Besides exploratory drilling, nondestructive geophysical techniques are efficient tools for investigating and predicting lithologic and structural heterogeneities for distances of up to several hundred meters from the tunnel wall. Among these, seismic imaging is the most effective because of its relatively deep penetration range and high spatial resolution.

Conventional tunnel seismic prediction systems operate as follows (Figure 1): Body waves (P- and S-waves) are excited at the sidewalls or at the face of the tunnel boring machine (TBM). These signals are reflected or scattered at geologic heterogeneities, e.g., cataclastic fault zones, and received by receivers placed in boreholes around the tunnel or at the head of the TBM. The seismic velocity field around the tunnel can be derived from the first arrivals by tomography. The spatial location of the discontinuities is usually estimated by reflection tomography or by migration. The success, resolution, and the prediction range of seismic imaging methods depend on the acquisition geometry, as well as on the degree of inhomogeneity of the rock mass.

Different tunnel seismic prediction systems have been applied since the early 1990s in tunneling projects worldwide. For tunnel construction in soft ground, the so-called sonic soft-ground probing system (SSP) has been developed (Kneib et al., 2000). SSP uses a high-frequency, P-wave vibroseis source and accelerometers on the cutter head of the TBM. The data are acquired while drilling is taking

Manuscript received by the Editor 24 November 2006; revised manuscript received 12 July 2007; published online 26 October 2007.
[1]TU Bergakademie Freiberg, Institut für Geophysik, Freiberg, Germany. E-mail: tbohlen@geophysik.tu-freiberg.de; stefan.jetschny@geophysik.tu-freiberg.de.
[2]Kiel University, Institute of Geosciences, Kiel, Germany. E-mail: ulrich.lorang@gmx.net; rabbel@geophysik.uni-kiel.de; cmu@geophysik.uni-kiel.de.
[3]GeoForschungsZentrum Potsdam, Environmental Geotechnique, Potsdam, Germany. E-mail: rudi@gfz-potsdam.de; slueth@gfz-potsdam.de.

place. SSP provides an image of the next few tens of meters ahead of the cutting face by migration of P-wave reflections.

Other systems apply seismic-while-drilling by using the noise of the TBM (Petronino and Poletto, 2002). Receivers are mounted on the TBM and behind it along the tunnel wall. The signals of the TBM pilot receivers are crosscorrelated with the remote receivers to derive the arrival times of the reflection events from ahead of the drilling front. Ashida (2001) uses both tunnel blasting and the TBM vibrations as seismic sources. He shows that imaging ambiguities can be reduced by using the direction of incidence of body waves in the migration process.

The commercialized tunnel seismic prediction (TSP) system (Dickmann and Sander, 1996) uses a system of as many as 30 explosive charges in boreholes in the tunnel sidewall as seismic sources and up to four 3-C accelerometers installed in boreholes as receivers. The TSP software identifies reflected body wave events from ahead, by their apparent velocities, and migrates them to the reflection points ahead of the construction. Another method, named in-tunnel horizontal seismic profiling (HSP), uses a source and receiver geometry as in a surface refraction seismic survey (Inazaki et al., 1999). The in-tunnel seismic data are processed in the same way as vertical seismic profiling (VSP) data. Reflection tomography is used in a system called true reflection tomography (TRT) (Neil et al., 1999). In the TRT system, body waves are excited by a sledgehammer applied at the tunnel face and at the sidewalls near the face. Accelerometers are located at the crown and on the sidewalls.

Since 1999, the concept of an integrated seismic imaging system (ISIS) has been developed (Borm et al., 2003a, b). A repetitive pneumatic hammer is applied every meter along lines on the sidewall behind the tunnel face. ISIS data acquisition is performed by means of 2-m long standard rock anchors which contain 3-C geophones at their tips. The seismic velocity field around the tunnel is derived by first arrival tomography (Giese et al., 2005). The migration of the seismic data uses the polarization information of the 3-C data to distinguish between P- and S-waves, and to decrease imaging ambiguities (Lüth et al., 2005).

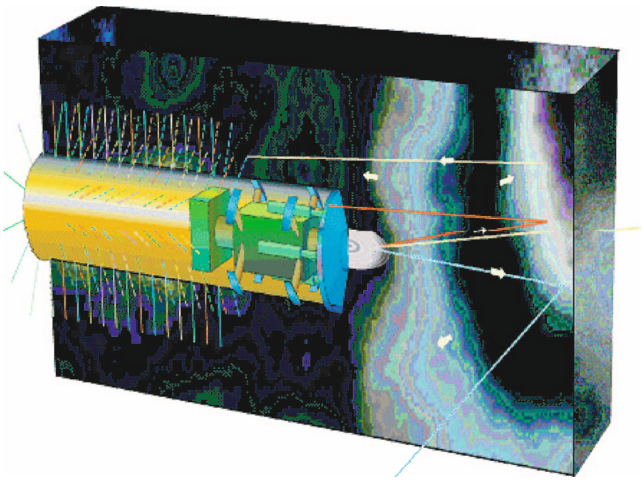

Figure 1. The situation of seismic imaging ahead of and around a tunnel. Conventional approaches use body waves (P- and S-waves) that are reflected and/or backscattered at geologic heterogeneities. Sources and receivers are either placed in the cutter head or behind the head of the tunnel boring machine (TBM). In typical underground constructions, tunnel diameter may vary between 3 and 15 m.

In this work, we suggest a new imaging strategy that has been discovered by 3D elastic finite-difference modeling. It utilizes Rayleigh waves that are converted into body waves at the head face of the tunnel. The new wave paths are illustrated in Figure 2. The Rayleigh waves are generated by a seismic source (e.g., hammer or explosion) behind the head of the TBM. They propagate along and around the tunnel, and arrive at the tunnel-head face where they are converted into body waves (P- and S-waves). Because of the conversion at the tunnel head face, this interface acts like a body-wave source that is triggered by the direct Rayleigh wavefield. After emission, the converted body waves are reflected at heterogeneities and are partly converted back into Rayleigh waves. These Rayleigh waves travel backward along and around the tunnel wall and are recorded by the receivers (geophones or accelerometers), which are located behind the tunnel face. One main advantage of this approach is that neither the sources nor the receivers need to be installed at the front face to use it as a transceiver of body waves. Source and receivers may be placed behind the cutter head and shield of the TBM, which keeps the interference with the ongoing excavation process to a minimum.

This paper is organized as follows. First, we investigate the efficiency of Rayleigh wave to body wave conversion at the (front) tunnel face (and vice versa) through a series of numerical-modeling experiments based on 3D finite-difference viscoelastic modeling. We describe in detail the complex wavefields involved in the conversion process and analyze the influence of the shape of the front tunnel wall, the role of phase velocity dispersion caused by the excavation zone, and the efficiency of the conversion as a function of the orientation of fault zone interfaces ahead of the construction. We then describe a simple and robust technique for detecting fault zones ahead of the underground construction. This method is successfully applied to synthetic data and also works well when applied to a field data example.

3D MODELING

The objective of our 3D elastic modeling is to understand the complex wavefields which contribute to the conversion of Rayleigh-to-body waves and vice versa. The efficiency of the conversion, and the complex wavefield involved, are first analyzed using a series of snapshots of the 3D seismic wavefield. We then study the effects of the shape of the head face, the role of phase velocity dispersion caused by the excavation damage zone, and finally the transceiver characteristics of the front face.

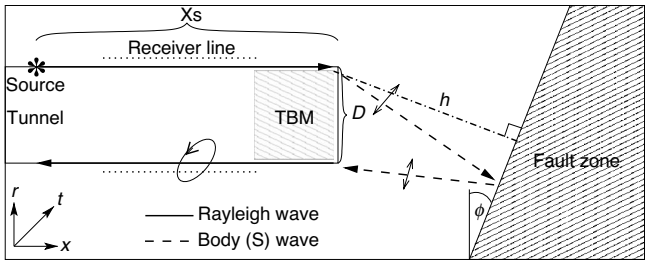

Figure 2. Wave path of Rayleigh-to-body wave (S-wave) conversion at the tunnel face. The face acts as a secondary S-wave source triggered by the direct Rayleigh wave. Reflected S-waves are converted back into Rayleigh waves. Arrows indicate the particle motion of waves. In typical underground constructions tunnel diameter may vary between 3 and 15 m.

The modeling is performed using a parallelized 3D viscoelastic finite-difference (FD) method (Bohlen, 2002). In this algorithm, the velocity stress formulation of the wave equation is discretized using second-order spatial and second-order temporal FD operators on a (standard) staggered grid (Virieux, 1986; Levander, 1988; Robertsson et al., 1994). The free surface of the tunnel is not treated explicitly, i.e., no explicit boundary conditions are applied. As shown by Bohlen and Saenger (2006), the free surface condition can be fulfilled with sufficient accuracy using second-order spatial FD operators, if the elastic moduli and density inside the tunnel are set to the corresponding parameters of air and if a certain averaging of material parameters is performed. Higher-order operators, e.g., fourth-order operators, are not applicable if free surfaces are modeled implicitely, i.e., treated as an ordinary geologic interface.

Diagrams of waveforms and raypaths are presented with respect to a local *x*-*r*-*t* Cartesian coordinate system where *x* represents a coordinate parallel to the tunnel axis, *r* is directed orthogonally to the tunnel wall into the rock formation, and *t* is tangential to the tunnel wall (Figure 2). Note that Rayleigh waves traveling along the tunnel wall in a direction parallel to the tunnel axis would be recorded on the *x*- and *r*-components only.

In our simulations, we consider a tunnel with a diameter of 10 m surrounded by a homogeneous crystalline rock mass. In front of the tunnel, we place a fault zone characterized by low velocities and significant absorption. The values of the elastic material parameters of the model constituents are listed in Table 1. We simulate the acquisition geometry shown in Figure 2. Seismic waves are excited by a point force (hammer) applied in the *r*-direction on the top sidewall of the tunnel. The source wavelet is a Ricker signal with a center frequency of 500 Hz and a maximum frequency of approximately 1000 Hz. The 3-C receiver line lies parallel to the tunnel axis on the same side as the shot. The receivers are "drilled" 2 m into the formation. They record the particle velocity field so that the synthetic data are comparable to geophone data.

In the FD simulations, we use a grid spacing of 0.2 m. The smallest wavelength of the Rayleigh wave is thus discretized with approximately 15 grid points guaranteeing sufficient accuracy for Rayleigh-wave simulations along free surfaces (Bohlen and Saenger, 2006). Larger grid spacing would lead to scattering of the Rayleigh wave at the staircases of the tunnel surface.

Absorbing frames with a width of 5 m are installed around the entire grid (Cerjan et al., 1985). A typical model grid has a size of 400 $\times$ 256 $\times$ 256 grid points in the *x*-, *y*-, and *z*-directions, respectively. A typical simulation requires approximately 2.5 hours on 32 CPUs of a Linux cluster.

To separate between P- and S-waves in the snapshots of the wavefield, we calculate the divergence and the magnitude of the curl of the particle velocity field (Dougherty and Stephen, 1988). The motivation for this is as follows. According to Morse and Feshbach (1953) the energy of P- and S-wave particle velocities is, respectively,

$$E_p = (\lambda + 2\mu)(\mathrm{div}(\mathbf{v}))^2 \quad \text{and} \quad E_s = \mu|\mathrm{rot}(\mathbf{v})|^2. \quad (1)$$

The Lamé parameters are λ and μ, and $\mathbf{v}$ is the particle velocity vector. To preserve the divergence and curl sign information, while showing relative compressional and shear particle velocity amplitudes, we plot the following quantities:

$$e_p = \mathrm{sign}(\mathrm{div}\mathbf{v})E_p^{1/2} \quad \text{and} \quad e_s = \mathrm{sign}(\mathrm{rot}\mathbf{v}\,.\,t)E_s^{1/2}, \quad (2)$$

where sign(rot$\mathbf{v}$. t) is the sign of the component of rot($\mathbf{v}$) that is oriented transverse (perpendicular) to the plane that includes the source and receivers, and the tunnel axis. The magnitudes of e_p and e_s are proportional to the magnitudes of the P- and S-wave particle velocities, respectively. Note that Rayleigh waves contain both a P- and S-wave component and therefore show up on both quantities of equation 2.

In our first simulation, we define a fault zone interface oriented perpendicular to the tunnel axis. The temporal development of the P-wave (divergence) and S-wave component (curl) within the *x*-*y*-plane, as defined in equation 2, is shown in Figure 3. In the beginning (Figure 3, 1–5 ms), we observe the excitation of P- and S-waves that is typical for a point force. P-waves radiate mainly to the sides (perpendicular to the tunnel axis), whereas S-waves propagate mainly parallel to the axis into the direction of drilling. Similar radiation characteristics are also observed for point forces applied on planar-free surfaces.

Because most of the P-wave energy is directed sidewards, the P-waves seem to be of limited use for looking ahead. However, a Rayleigh wave travels along and around the tunnel with a velocity of approximately 92% of the S-wave speed. It reaches the face after approximately 7 ms. Here, most of its energy is converted into an S-wave propagating further ahead. This forward-radiated S-wave exhibits very high amplitudes. The conversion of the Rayleigh wave into a P-wave is much less efficient. The weakly converted P-wave radiates mainly perpendicularly to the tunneling direction (Figure 3, 12 ms). Therefore, P-waves converted from Rayleigh waves do not seem to be well suited for imaging structures ahead. At the crown of the head face, the direct Rayleigh wave is scattered into all wave types, i.e., Rayleigh waves, P-waves, and S-waves. The scattered Rayleigh waves propagate around the front face and also backward. The high-amplitude S-wave, which was generated by the direct Rayleigh wave, arrives at the fault zone after approximately 18 ms. Here, it is reflected as both P- and S-waves. The reflected S-wave exhibits higher amplitudes than the mode-converted reflected P-wave (Figure 3, 20–25 ms). As the reflected S-wave reaches the tunnel face again, most of its energy is converted back into a Rayleigh wave that travels backward along the tunnel. This back-conversion of S-waves into Rayleigh waves at the tunnel face is also very efficient for dipping fault zones, as will be shown later. We name this phase RSSR to indicate the wave path and history of this event.

The synthetic seismograms for this simulation, shown in Figure 5, reveal that the RSSR-wave is the dominant reflection event from the fault zone. Highest amplitudes are observed on the *r*-component, i.e., perpendicular to the tunnel axis and the tunnel wall. The seismograms also show backward-traveling Rayleigh waves scattered at the crown of the face (indicated by RR1 and RR2), and a circulating

Table 1. Material properties used in the simulations: Given are the values of density ρ, seismic velocities v_p and v_s, and quality factors Q_p and Q_s for P- and S-waves, respectively.

Parameter	Tunnel	Rock	Fault-zone
ρ (kg/m^3)	1.25	2200.0	1800.0
v_p (m/s)	0.0	5700.0	4000.0
v_s (m/s)	10^{-6}	3400.0	2400.0
Q_p	∞	500.0	100.0
Q_s	∞	500.0	100.0

Rayleigh wave (CR) that is generated at the source point and then propagating around the axis of the tunnel. Hodograms of the particle motion of the RSSR wave derived from time-windowed seismograms of Figure 5 are shown in Figure 6. Figure 6 reveals that the RSSR wave has an elliptical motion in the *x*-*r* plane and very small movement perpendicular to this plane (transverse direction). Its motion is similar to the motion of the direct Rayleigh wave (analysis not shown).

The identification of the strong direct and backward-propagating (RSSR) waves as Rayleigh waves is based on the following wave attributes derived from the synthetic seismograms: (1) The wave amplitudes are large near the tunnel wall and decay exponentially into the rock formation. The propagation direction, parallel to the tunnel axis, is orthogonal to the direction of amplitude decay (Figures 3 and 4). (2) The wave is polarized elliptically in the *x*-*r* plane (Figure 6). (3) Its propagation velocity is 92% of the shear wave velocity of the

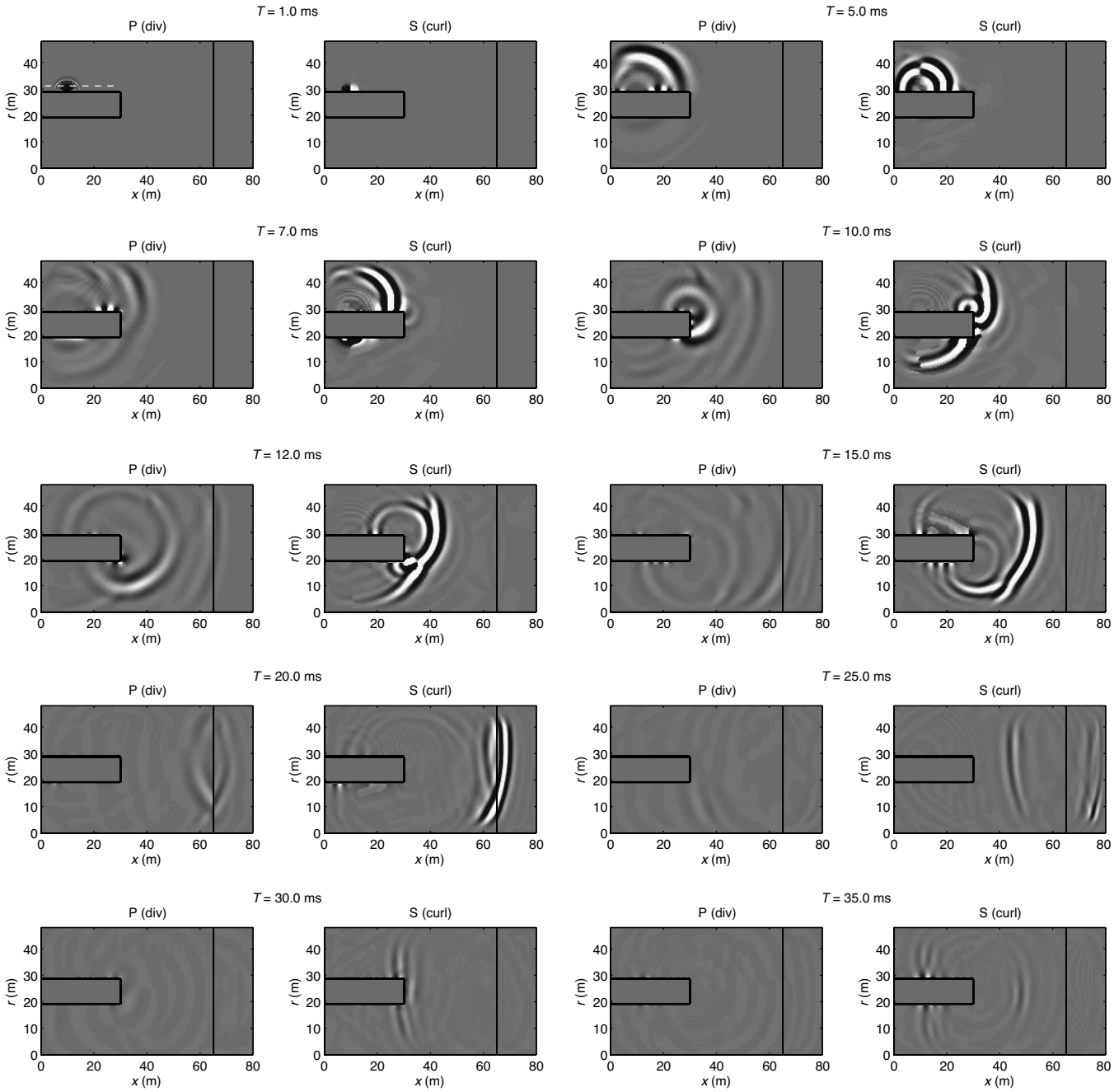

Figure 3. Snapshots of the P-wave components (divergence) and S-wave components (curl) (equation 2) showing the Rayleigh-to-body wave conversions at the front tunnel face. A Rayleigh wave is excited by a point force at the tunnel wall (1 ms) and then propagates along and around the tunnel. When it arrives at the front face (10 ms), it is converted mainly into a S-wave, which is then reflected at the fault zone. The backward-traveling reflected S-wave converts back into a Rayleigh wave (30 ms).

rock formation, such as would be expected for Rayleigh waves at the surface of a homogeneous half-space. (4) In this synthetic example, the Rayleigh-type wave shows no dispersion because the S-wave velocity of the rock formation was assumed to be homogeneous and the tunnel radius is larger than the wavelength.

Forward scattering

To investigate the relative contributions of the direct S-wave and the Rayleigh wave in the forward-scattered wavefield in more detail, we performed a different simulation in which we extended the length of the tunnel considerably so that the direct Rayleigh and S-wave separate in space and time. In this simulation, the propagation distance along the wall was 120 m corresponding to 12 times the tunnel diameter. All other simulation parameters remain the same.

Two snapshots showing the wavefield before and after the conversion are displayed in Figure 4. The different wave types can now be distinguished. One can identify the Rayleigh wave at the tunnel wall (R), the direct S-wave (S), the Rayleigh-to-P converted wave (RP), and the Rayleigh-to-S converted wave (RS). Figure 4 reveals that the direct S-wave has low amplitudes near the tunnel. Also, no scattering of the direct S-wave at the front face is observed. Thus, the contribution of the direct S-wave (S) into the forward-radiated wavefield is small. In contrast, the Rayleigh wave has high amplitudes near the tunnel wall and the conversion into S-waves (RS) at the front face is strong. The Rayleigh-to-P converted wave (RP) exhibits much smaller amplitudes. This simulation example suggests that, for the considered frequency range and tunnel diameter, the forward-propagating S-waves mainly originate from the scattering of the Rayleigh wave at the tunnel face.

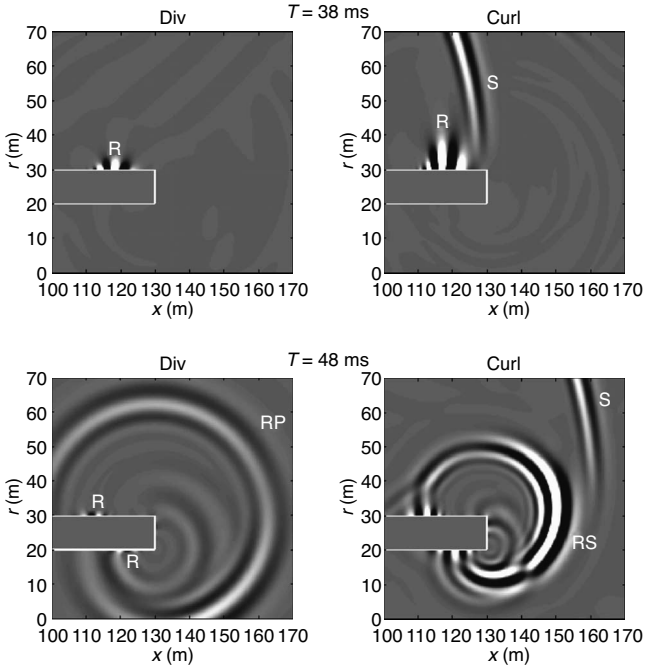

Figure 4. Wavefield scattering at the front face. The direct Rayleigh wave (R) is converted into P- (RP) and S-waves (RS). The contribution of the direct S-wave (S) into to forward-scattered wavefield is small.

Shape of the front tunnel face

During the drilling process, the shape of the front face varies with rock types. Moreover, in reality, the corners are not as sharp edged as in the FD models, so the Rayleigh wave scattering at these corners may be less pronounced in practice. Therefore, we studied the effect of tunnel-wall topography of the front face. We assumed elliptical shapes of the front face and varied the size of one axis of the ellipse. As an example, Figure 7 shows the forward-radiated wavefield when

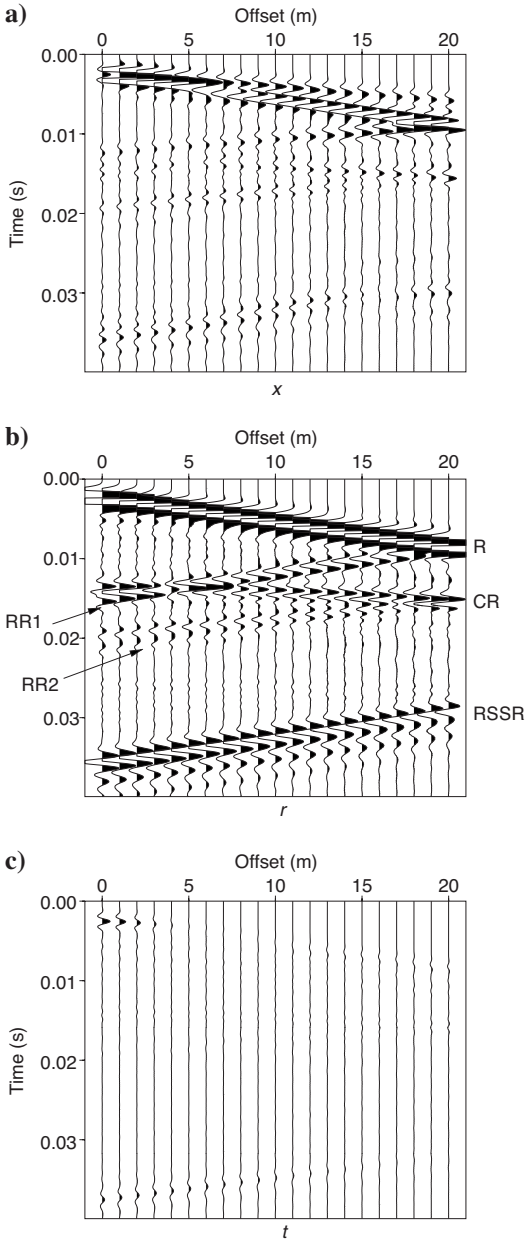

Figure 5. Seismograms corresponding to the snapshots shown in Figure 3. The receiver line is indicated by a white dashed line in Figure 3 (1 ms). Amplitudes are multiplied by time to correct for geometrical spreading. (a), (b), and (c) show the inline (x), radial (r), and tangential (t) component of particle velocity, respectively. R denotes the direct Rayleigh wave. RR1 and RR2 are Rayleigh waves scattered at the crown of the face. CR is the direct circulating Rayleigh wave, and RSSR is the S-wave reflection at the fault zone, which is recorded as a Rayleigh wave.

the front face exhibits a bulge of 2 m (20% of tunnel diameter). The comparison with Figure 3 reveals that the forward-radiated wavefield, i.e., the P- and S-waves excited by the direct Rayleigh wave, remains nearly unchanged. The same is observed for bulges up to 5-m extension. The main difference to a plain face (Figure 3), is that the scattering at the edges (crown) of the face is much less pronounced leading to smaller amplitudes of the backward-propagating Rayleigh waves that are generated by Rayleigh-wave scattering (events annotated with RR1 and RR2 in Figure 5). Also the backward-conversion of S-waves into Rayleigh waves does not vary notably for different face shapes. Altogether, we therefore conclude that topography of the front face of realistic extensions does not influence the transceiver characteristics of the front face. Real conditions in tunneling operations exert an even positive influence as scattering at the corners is less pronounced.

Excavation damage zone

The crystalline rock around the tunnel is significantly altered during drilling of the tunnel. The width of the so-called excavation damage zone (EDZ) varies, depending on the excavation method and the ambient stress regime around the tunnel: between a tenth of the tunnel diameter for a tunnel boring machine (TBM) and up to one diameter for conventional tunneling by drilling or blasting (Giese et al., 2005; Schuster et al., 2001). The EDZ is especially characterized by strong gradients in the elastic material parameters, and should thus cause a significant frequency dependence of the phase velocities of Rayleigh waves (RSSR waves) because these are highly sensitive to shallow S-wave velocity variations. Dispersion means a frequency-dependent arrival time of RSSR waves and consequently leads to a variation of phase with distance (waveform broadening) and thus to a poor stacking result, if conventional processing and migration routines are applied.

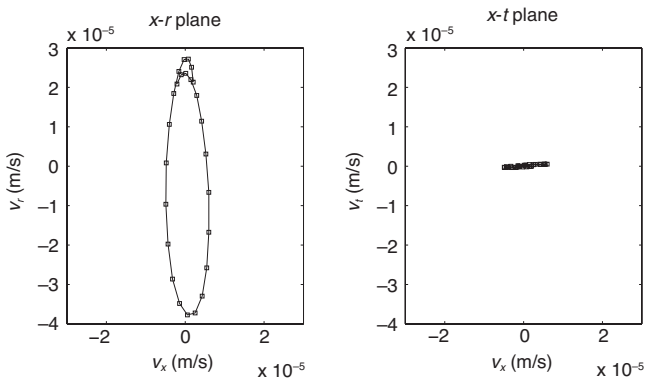

Figure 6. Particle motion of the RSSR wave in the *x-r* (left) and *x-z* plane (right). The hodograms were derived from the seismograms of Figure 5. The RSSR wave has elliptical particle motion in the *x-r* plane.

To study the effects of dispersion caused by the EDZ, we introduce a damage zone around the tunnel having an extension of 10 m (one tunnel diameter) and S-wave velocities increasing from 1800 m/s at the tunnel wall to 3400 m/s in the undisturbed region. This results in an S-wave velocity gradient of 160 m/s/m in the EDZ which can be regarded as strong, but realistic. Similar S-wave gradients have been derived by S-wave first arrival tomography in the Faido adit of the Gotthard base tunnel (Giese et al., 2005). We assume a constant ratio of P- to S-wave velocity of $\sqrt{3}$ throughout the model and a density gradient of 700 kg/m^3/m in the EDZ. The parameters of the undisturbed region are given in Table 1. The wavefield that was obtained using the acquisition geometry described above is shown in Figure 8 where the total source to tunnel face offset is now 75 m. The seismograms correspond to the particle velocity component perpendicular to the tunnel surface. In comparison with Figure 5, the direct, circulating (CR), and reflected Rayleigh waves (RS, RSSR) experience significant dispersion leading to a phase variation with distance. In the direct wavefield, the fundamental mode (FM) that travels with lowest phase velocities exhibits highest amplitudes. The amplitudes of the direct higher modes (indicated by HM in Figure 8) are weaker, but still visible in the direct wavefield. All modes can be identified in the circulating Rayleigh-waves (CR) as well. Because of the broad range of phase velocities (approximately 1800 to 3400 m/s) the circulating (faster) higher modes interfere with the (slower) directly propagating fundamental

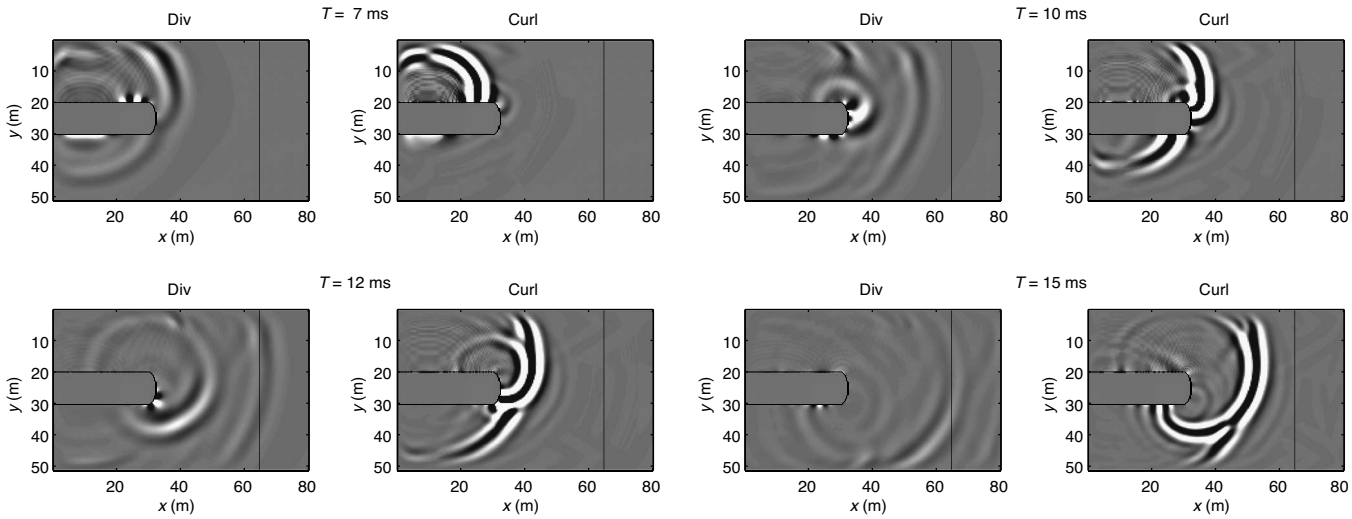

Figure 7. Snapshots of the P-wave components (divergence) and S-wave components (curl) showing the Rayleigh-to-body wave conversions in the case of an ellipsoidal front face. The head face has a bulge of 2 m. Scattering of the Rayleigh waves at the edges is less pronounced. The conversion of Rayleigh waves into forward-radiating body waves remains nearly unchanged.

mode after 50 m corresponding to five tunnel diameters only. In the presence of a significant EDZ, the Rayleigh wave arriving at the front face is thus composed of multiple modes that have propagated along different paths, i.e., directly and around the curved tunnel surface. The backward-propagating Rayleigh waves consequently are composed of many modes as well. A dispersion analysis reveals that the reflection at the front face (RS) mainly propagates as the fundamental mode, whereas the RSSR reflections are dominated by higher modes. A further theoretical analysis of the transceiver characteristics for multimodal Rayleigh waves is, however, beyond the scope of the paper and will be an important topic for future work.

For such numerical and theoretical investigations, it is important to check to see if the dispersion of the observed Rayleigh waves propagating along or around the curved tunnel wall is similar to the dispersion of the actual Rayleigh waves traveling along a planar free surface in a horizontally layered half-space. This is because, for the latter medium, various methods for the calculation of Rayleigh-wave dispersion curves (Green's functions) are available and could thus be used to describe the interface waves around a tunnel as well. Is it justified that we call the interface waves at the tunnel surface *Rayleigh waves*? If so, the wavefield arriving at the front face could be considered as a superposition of conventional Rayleigh waves that have reached the front face along different travel paths.

To evaluate if the curvature of the surface can be neglected in the frequency range of a typical hammer blow (200–1500 Hz), seismograms for a layered half-space with subsurface properties corresponding to the parameters of the EDZ have been computed and are compared with the tunnel interface waves in Figure 9. The direct comparison of the signals in Figure 9, and a detailed analysis of slowness-frequency representations of the shot gathers, suggests that the dispersion characteristics of Rayleigh waves along a planar free surface and a curved tunnel wall are identical. The main difference between the two cases are the circulating Rayleigh-wave modes that are absent in a horizontally stratified half-space. We therefore conclude that in our case, a curved tunnel and a planar free surface produce the same Rayleigh-wave dispersion. Hence, we can use the reflectivity method (Wang, 1999) for a stratified half-space to calculate the slowness-frequency spectrum (Green's function) to study the frequency range of the excited modes. The slowness-frequency spectrum for the EDZ described above is shown in Figure 10. The local amplitude maxima, in the slowness-frequency spectrum, correspond to the dispersion curves of the Rayleigh wave. Figure 10 reveals that mainly the fundamental mode and two higher modes contribute to the observed wavefield in the seismic frequency range of a typical hammer blow (dashed line in Figure 10). The fundamental mode is excited below approximately 800 Hz whereas the higher modes are dominant above 800 Hz. The variation of fundamental

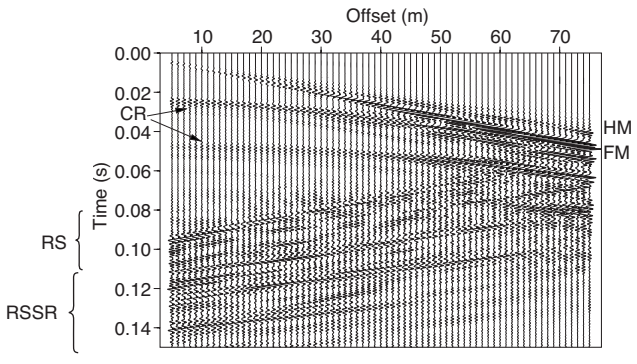

Figure 8. Dispersed Rayleigh-wave modes propagating along and around the tunnel in the presence of an EDZ with an extension of 10 m and a shear-wave velocity gradient of 160 m/s/m. FM and HM denote the directly propagating fundamental and higher modes, respectively. The circulating modes are indicated by CR. The Rayleigh waves reflected at the head face (RS) and RSSR reflections at the fault zone interface are composed of multiple modes as well. Amplitudes are gained linearly with time.

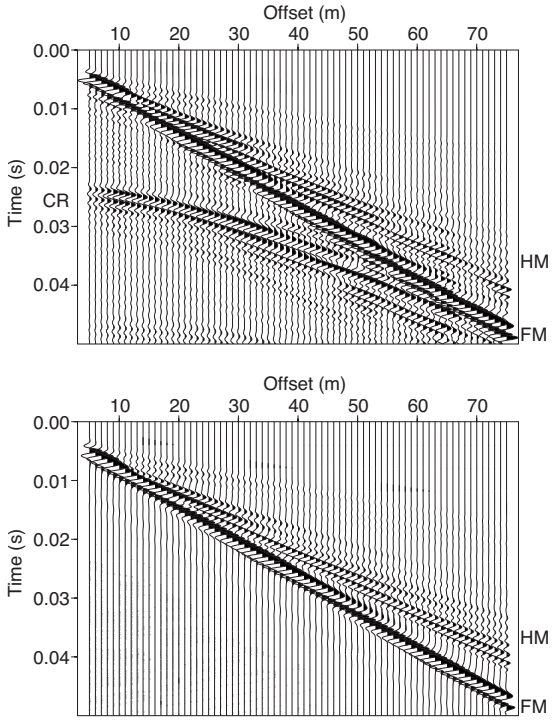

Figure 9. Comparison between direct Rayleigh waves propagating along and around a tunnel (top) and along a planar free surface (bottom). A shear-wave velocity gradient of 160 m/s/m perpendicular to the interface is assumed (EDZ). Seismograms are trace-normalized.

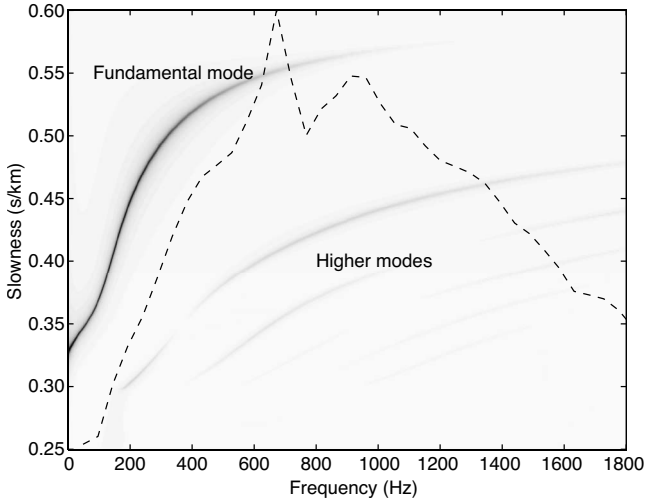

Figure 10. Dispersion of Rayleigh waves traveling in an EDZ with an extension of 10 m and a shear-wave velocity gradient of 160 m/s/m. The amplitude spectrum of a recorded typical hammerblow is plotted as a dashed line.

mode phase velocity with frequency is most significant below approximately 400 Hz. It must be noted, however, that the slowness-frequency spectrum of Figure 10 represents a typical, but single example only. The elastic parameters of the EDZ are certainly strongly site dependent and, consequently, are the excitation and phase velocities of the Rayleigh-wave modes. We thus must expect a broad variety of slowness-frequency spectra as observed in shallow seismic investigations in engineering geophysics.

Dipping reflectors

In the previous example (Figure 3), we investigated the case in which the normal vector of the fault zone interface is oriented parallel to the tunnel axis, i.e., a dip angle of 0° ($\phi = 0°$). In this direction, we observed efficient conversion of Rayleigh-to-S-waves and vice versa at the tunnel head face, resulting in high amplitudes of the RSSR wave (Figure 5). However, the amplitudes of the forward-radiated S-wave (Rayleigh-to-S-wave conversion), as well as the backward-conversion (S- to Rayleigh wave) depend upon the ray directions of the transmitted and received S-wave, respectively. To quantify the angle dependency of the RS and SR conversion, we study the amplitudes and waveforms of the RSSR wave for different dip angles of the fault zone interface. The results are summarized in Figure 11. The interface is positioned in a way that it produces an S-S reflection angle of 0° for all orientations of the interface. Amplitude

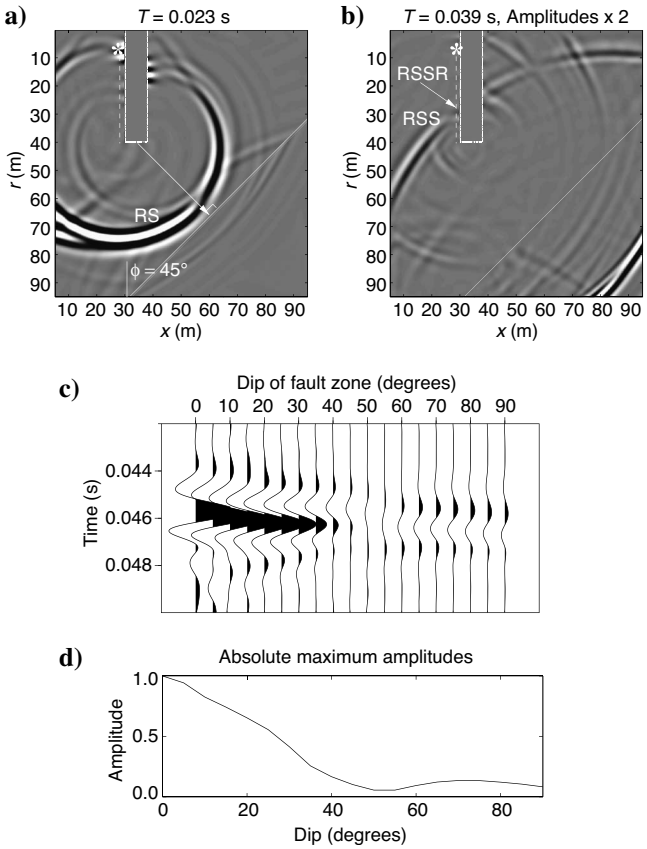

Figure 11. Detectability of interfaces as a function of their orientation. (a) and (b) S-wave (curl) snapshots for a dip angle of $\phi = 45°$. Note the phase reversal of the emitted RS wave indicated by the white arrow. (c) Waveforms of particle velocity of the RSSR event recorded along the receiver line (dashed line in (a)). (d) Maximum absolute amplitude of the seismograms shown in (c).

variations can thus be attributed to the transceiver characteristics of the tunnel head face. We choose a constant travel path of the reflected S-wave of $h = 40$ m (Figure 2) between the front tunnel face and the interface.

Let us first consider the snapshot of the S-wavefield in the case of a dip angle of $\phi = 45°$ shown in Figure 11a. The forward-radiated RS wave exhibits highest amplitudes in the forward direction (parallel to the tunnel axis), as discussed above. The amplitudes of the RS wave are also relatively high for radiation angles around 90° (perpendicular to the tunnel axis). An interesting finding is the observation of a phase reversal of the transmitted RS wave around 45°. The corresponding ray direction is indicated by a white arrow in Figure 11a. In the vicinity of this phase reversal, the emitted RS wave exhibits minimum amplitudes, which in turn leads to low amplitudes of the reflected RSS wave and backward-converted Rayleigh wave (RSSR wave) that propagates backward along the tunnel wall (Figure 11b). The waveforms and the maximum amplitudes of the RSSR event recorded at the tunnel wall, coinciding with the shot location, are shown in Figure 11c and d, respectively, for different dip angles of the interface. The time axis window in Figure 11c thus corresponds to the arrival time of the RSSR wave at the shot position (indicated by a star in the snapshots). Highest amplitudes are recorded when the interface normal is oriented parallel to the tunnel axis ($\phi = 0°$ in Figure 11c). The phase reversal of the emitted S-wave leads to minimum amplitudes of the RSSR event around 45°. From Figure 11d, we conclude that interfaces with dip angles exceeding 30° with respect to the tunnel axis may be difficult to detect in real field observations. The detectability is best for dipping angles of about 0°. For negative angles (not analyzed in Figure 11), the forward-propagating converted Rayleigh wave (RS) exhibits no phase reversal and therefore a good detectability can be achieved for dipping angles up to −90°.

PROCEDURE FOR DETECTING INTERFACES AHEAD

The modeling results presented in the previous section showed that the head face can act as a transceiver for S-waves that is triggered by the direct Rayleigh wave. In the presence of an EDZ, the direct and backward-traveling Rayleigh waves are composed of multiple modes that propagate with different frequency-dependent velocities. In the following, we outline a procedure for estimating the distance h between the head face and the reflector. Consider the acquisition geometry and the wave path depicted in Figure 2. If we denote the distance between the shot and the head face as x_s, the frequency-dependent traveltime curve $t_{nm}(x,f)$ of a forward-propagating mode n and a backward-propagating mode m reads, for source and receivers on opposite walls

$$t_{nm}(x,f) = p_n(f)x_s + v_s^{-1}\left(D^2 + 4h^2 - 4hD\sin(\phi)\right)^{1/2} + p_m(f)(x_s - x), \quad (3)$$

where $p_n(f)$ denotes the phase slowness (dispersion curve) of a forward-propagating Rayleigh-wave mode, and $p_m(f)$ the phase slowness of a backward-propagating mode. The S-wave velocity v_s is ahead of the tunnel which is assumed to be constant. The temporal frequency is f. D is the diameter of the front face and ϕ is the dipping angle of the fault zone interface (Figure 2).

To improve the signal-to-noise ratio of a backward-propagating RSSR mode by stacking, we must first correct the dispersion of the

corresponding mode by deconvolution. For a description of this procedure, we separate the frequency dependence of the phase slowness

$$p_n(f) = p_{n,c} + \delta p_n(f) \tag{4}$$

$$p_m(f) = p_{m,c} + \delta p_m(f), \tag{5}$$

where $p_{n,c}$ and $p_{m,c}$ are the minimum (cut-off) slowness of the forward- and backward-traveling modes, respectively. For higher modes $(n,m \geq 1)$ the cutoff slowness is

$$p_{n,c} = p_{m,c} = v_{s,b}^{-1} \quad (n,m \geq 1), \tag{6}$$

where $v_{s,b} \approx v_s$ denotes the background velocity around the tunnel beyond the EDZ. For the fundamental mode $(n,m = 0)$, a good estimate in crystalline host rocks (with Poisson ratios of approximately 0.25) is

$$p_{o,c} = (0.92 v_{s,b})^{-1}. \tag{7}$$

By inserting equations 4 and 5 into equation 3 we obtain

$$t_{nm}(x,f) = (p_{n,c} + p_{m,c})x_s + v_s^{-1}(D^2 + 4h^2 - 4hD\sin(\phi))^{1/2} + (\delta p_n(f) + \delta p_m(f))x_s - p_m(f)(x). \tag{8}$$

The first two terms in equation 8 denote the frequency independent traveltime of the RSSR mode. The third term describes an offset-independent dispersion and the last term is the dispersion of the backward-propagating mode. To correct the latter two effects, we apply a frequency-dependent traveltime correction in the frequency domain by multiplying the phase spectra of the seismograms with $-2\pi f(\delta p_n(f) + \delta p_m(f))x_s - p_m(f)(x))$. The dispersion curves that are required for this deconvolution may be derived by a dispersion analysis of the direct wavefield (McMechan and Yedlin, 1981; Forbriger, 2003). If the EDZ exhibits lateral variations of the elastic properties, the functions $p_n(f)$ and $p_m(f)$ represent effective slowness that is averaged over the travel path of the Rayleigh wave. These may be obtained, e.g., by averaging local dispersion curves along the tunnel (Bohlen et al., 2004), or by analyzing phase differences between the recordings at far offsets and an zero offset trace.

After such a deconvolution (dispersion correction) the RSSR events are free of dispersion and the arrival time of an RSSR mode becomes independent of frequency and distance x:

$$t_{nm}^{\text{deco}} = (p_{n,c} + p_{m,c})x_s + v_s^{-1}\big(D^2 + 4h^2 - 4hD\sin(\phi)\big)^{1/2}. \tag{9}$$

After deconvolution, a backward-propagating RSSR mode thus arrives at time t_{nm}^{deco} for all receivers. We can now stack the deconvolved seismograms in a shot gather or common-receiver gather to enhance the signal-to-noise ratio of a specific mode. Other backward-propagating modes and body waves, that differ in their phase velocities, will be reduced significantly by the stacking process. Tests with synthetic data showed that it is not necessary to further reduce the other events prior to stacking, e.g., by *f-k* filtering, if a sufficient number of traces (greater than 10–15) contribute to the stacked seismogram. In field data, the required number of traces depends mainly on the signal-to-noise ratio and the range of offsets available.

If the receivers are located along the same side of the tunnel wall $(D = 0)$, the arrival time of an RSSR mode after deconvolution simply reduces to

$$t_{nm}^{\text{deco}} = (p_{n,c} + p_{m,c})x_s + 2hv_s^{-1}. \tag{10}$$

If we consider higher modes only, we simply obtain (using equations 4 and 5)

$$t_{nm}^{\text{deco}} = 2v_s^{-1}(x_s + h) \quad (n,m \geq 1), \tag{11}$$

and when considering fundamental modes only (using equation 7)

$$t_{nm}^{\text{deco}} = 2v_s^{-1}(x_s/0.92 + h) \quad (n,m = 0). \tag{12}$$

Deconvolved fundamental modes thus arrive slightly later than deconvolved higher modes.

In this acquisition geometry $(D = 0)$, we can explicitly determine the distance h between the face and the fault zone. From equation 10 we obtain

$$h = \frac{v_s}{2} t_{nm}^{\text{deco}} - \frac{1}{2}(p_{n,c} + p_{m,c})v_s x_s. \tag{13}$$

We may use equation 13 to convert the time axis t_{nm}^{deco} of the deconvolved and stacked seismogram to distance h from the head face to obtain a quick overview over the seismic energy that is reflected at certain distances. For each combination of modes (n,m), we obtain a different reflection response, if the corresponding modes are excited in the direct and the backward-going surface waves, respectively. High amplitudes would indicate distances ahead of the tunnel with strong S-S reflections and thus high S-wave impedance contrasts.

According to equation 3, it is not possible to determine both the dip ϕ of the interface and the distance h to the interface simultaneously from a single shot gather only. However, a recurrent application of the procedure described above, while the tunnel face approaches the fault zone, allows one to quantify the dip angle ϕ by analyzing the RSSR arrival times for different positions of the front face. Imagine that the tunnel face has been drilled by a distance $\triangle x$ into the x-direction (Figure 2). At each distance, we acquire a shot gather, apply the deconvolution, stack the data, and convert the time axis into distance h using equation 13. We compile all stacked traces to a gather which we name *RSSR-gather*. For each combination of forward- and backward-propagating modes (n,m), we obtain a separate RSSR-gather. The RSSR-gather mainly contains the S-S reflection amplitudes as a function of the face position x and the distance of the reflector h. If we denote the reduced distance to the fault zone by h', then the dip angle can be calculated from an RSSR-gather using the following geometric relation

$$\cos(\phi) = \frac{h - h'}{\triangle x} = \frac{\triangle h}{\triangle x} = \tan(\beta), \tag{14}$$

where β denotes the dip angle of the RSSR mode in the RSSR-gather. The procedure for estimating the distance h and the dip angle ϕ from RSSR-gathers is illustrated in the following section.

Application to synthetic data

Simple example

We first test the applicability of this approach for detecting structures ahead using synthetic FD data. In our first example, we neglect the dispersion of Rayleigh waves caused by the presence of the EDZ to better illustrate the method. We apply the traveltime correction and stack the seismograms shown in Figure 5b, on which the nondispersive RSSR wave is easily identified. To correct for the linear

moveout of the RSSR event, we automatically pick the maximum amplitude of each seismogram and then shift the data by the arrival time of the maximum amplitude. Alternatively, we could have applied a phase correction in the Fourier domain as described above. After the time shift, we mute the direct Rayleigh wave. The resulting seismograms are shown in Figure 12a. As expected from equation 10, the backward-propagating Rayleigh waves now arrive at the same time for all receivers. In the next step, the traces in Figure 12a are stacked and the time axis is scaled using equation 13. The stacked trace is shown in Figure 12b. The first two events in Figure 12b at $h \approx 0$ m and $h \approx 10$ m represent the Rayleigh waves, which are scattered at the crown of the face (Figure 3). The third event is the RSSR reflection from the fault zone. It exhibits by far the highest amplitudes. It shows up at $h \approx 35$ m, which corresponds to the true distance of the fault zone.

Application while drilling

If this procedure is repeated while drilling, i.e., for different distances between the face and fault zone, we can estimate the dip of the fault zone using equation 14. To illustrate this, we performed simulations in which we moved the tunnel face closer to a dipping fault zone (Figure 13, top). Again, an EDZ was not considered, i.e., the Rayleigh waves exhibit no dispersion. We assume a dip angle of the fault zone of $\phi = 35°$. For each face location, an FD simulation with the same absolute source and receiver positions is repeated. The tunnel face moves by a distance of 2 m between two simulations. Each shot gather is processed as shown in Figure 12. The resulting traces are plotted as a function of the face position x in Figure 13 (bottom). In this RSSR gather, we can clearly identify the RSSR event which approaches the RR1 wave (scattered at face edges) as the tunnel face approaches the fault zone. As expected, the distance h between the face and the fault zone interface decreases with increasing face position x. The angle β (Figure 13, bottom) in the RSSR-gather, between the face-scattered Rayleigh wave RR1 and the RSSR wave, is a measure of the dip angle of the fault zone (see equation 14). Here, we estimate the dip of the RSSR event to be $\beta = 39.3°$, the resulting dip of the fault zone thus is $\phi = \text{acos}(\tan(\beta)) \approx 35°$, which agrees well with the true value of 35°.

Application in the presence of an excavation damage zone

To test the performance of deconvolution and stacking in the presence of an EDZ, we apply the procedures on the multimodal Rayleigh wavefield shown in Figure 14. To simplify matters, and to better illustrate the applicability, we apply it on 2D synthetic data that are free of circulating Rayleigh waves (see also Figure 9). Figure 14a (left) shows the seismograms after deconvolution of the dispersion of the forward- and backward-propagating fundamental mode ($n = 0$, $m = 0$). After deconvolution, the backward-propagating fundamental modes that are reflected at the front face (indicated by RR) and the RSSR reflection at the fault zone ahead of the front face (indicated by RSSR) arrive at a constant time given by equation 12. The reflected signals exhibit no dispersion, i.e., the waveforms of the reflected signals are the same for all receivers. Stacking of the seismograms, shown on the right side of Figure 14a, thus yields clear events of the reflected fundamental modes. The amplitudes of other events, e.g., body waves and also the higher Rayleigh-wave modes, are significantly reduced by stacking because their arrival times and waveforms vary with receiver position. The deconvolution and stacking of the first higher mode is shown in Figure 14b. Here we correct for the first higher mode dispersion ($n = 1$, $m = 1$). As expected, we obtain a different stacking response. The stacked signals of RR and RSSR contain higher frequencies because of the higher-frequency content of the higher mode. The time axes of the stacked seismograms in Figure 14a and b (right) have been scaled to the distance ahead of the tunnel using equation 13. Both RSSR modes are reflected in a distance of 40 m ahead of the tunnel which agrees with the "true" distance of the fault zone assumed in the FD simulation.

The results for multimodal Rayleigh waves presented in Figure 14 are promising. They suggest that different reflection responses of interfaces ahead may be achieved for different combinations of for-

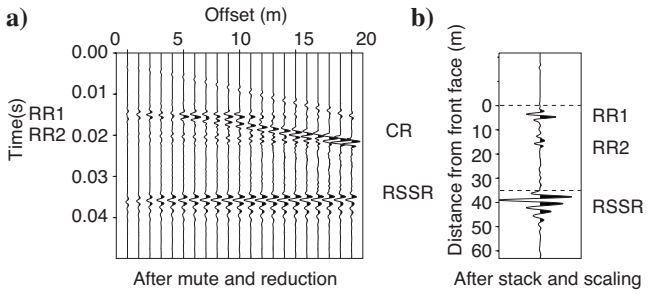

Figure 12. Estimation of fault zone distance using the input data shown in Figure 5b. (a) After time shift and removal of direct Rayleigh wave. (b) After stacking and time axis scaling (equation 13). Dashed lines correspond to the face location and the fault zone interface.

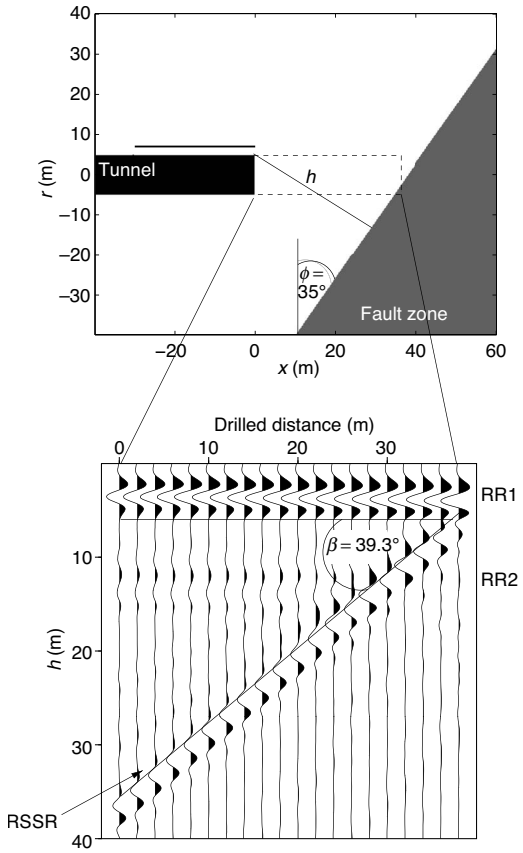

Figure 13. The dip angle ϕ as well as the reflector distance h can be derived from RSSR gathers (bottom) using equation 14.

ward- and backward-propagating modes (n, m). The synthetic tests show that when higher modes are involved, the stacked RSSR events exhibit higher frequencies that might lead to a better spatial resolution of structures ahead of the construction. Further investigation of optimal mode combinations and corresponding consequences for seismic imaging is, however, beyond the scope of this paper and will be a topic for future work.

FIELD DATA EXAMPLE

Motivated by the finite-difference modeling described above, the GFZ Potsdam, in cooperation with Amberg Technologies (AMT, Regensdorf, Switzerland), carried out seismic measurements in March 2005 at the tunnel face of the Piora adit near the Gotthard base tunnel (GBT) construction site (Figure 15a) (Lüth et al., 2007). The Piora adit had been excavated in the beginning of the construction of the GBT to explore the Piora Basin. The Piora Basin is characterized by extremely unstable sugar-like dolomite and more stable carbonatic-sulfatic rocks (Schneider, 1997). This structure is regarded as a particular challenge for the tunneling process. At the face of the Piora adit, two exploratory wells were drilled into the Piora Basin. Along the wells, the following rock units were found: Lucomagno Gneiss of the Penninic Gneiss zone for the first 40 m, 18 m of a kakiritic fault zone, about 230 m Triassic Piora Basin rocks, and crystalline series of the Gotthard Massif.

The seismic survey was carried out with two receivers and 76 source points (Figure 15b). At the source points, a pneumatic hammer developed by the GFZ Potsdam (Borm et al., 2003) was used to generate seismic signals. A description of data acquisition, processing and RSSR migration of the complete data set is presented by Lüth et al. (2007). In this modeling paper, we use the data on one tunnel wall only. Analogous to the synthetic data (Figure 5), we use the data of the right receiver, fixed circa 70 m behind the tunnel face and 35 source points (SP 42–76) along the right tunnel wall between the receiver and the tunnel face (Figure 15b).

The raw data and their processing and stacking results are shown in Figure 16. A dispersion analysis of the direct Rayleigh waves, that dominate the raw seismograms, revealed that the Rayleigh waves are nearly free of dispersion. The Rayleigh wave is excited between 200–400 Hz. In this frequency range, the dispersion that is caused by the EDZ thus seems to be negligible. In the raw data (Figure 16a), one can easily identify two backward-going waves that have the same apparent velocity as the direct Rayleigh wave. The first event is the Rayleigh wave reflection at the front face and the second is an RSSR reflection. Because the forward- and backward-propagating Rayleigh waves are free of dispersion, a dispersion correction by deconvolution is not necessary. We simply determine the arrival time of the direct Rayleigh wave and shift the traces by this time. Afterward, we mute the direct Rayleigh wave. The result is shown in Figure 16b. The backward-going Rayleigh waves arrive at the same time (flattened). The stacked seismogram, shown in Figure 16c, exhibits a clear event that corresponds to an RSSR reflection. The RSSR-stacked result is compared to the schematic rock-quality designation (RQD) profile along one of the above-mentioned exploratory wells (Figure 16d). The RQD value is a measure for the stability of the cored material (Deere and Deere, 1988). High values indicate stable rock masses, and low values indicate unstable rocks. The transition from the high RQD values of the Lucomagno Gneiss to the kakiritic zone with low RQD values at circa 40 m from the tunnel face correlates well with a strong signal in the RSSR stack in Figure 16c. This suggests that the recorded RSSR event corresponds to an SS reflection at the kakiritic zone of the Piora Basin.

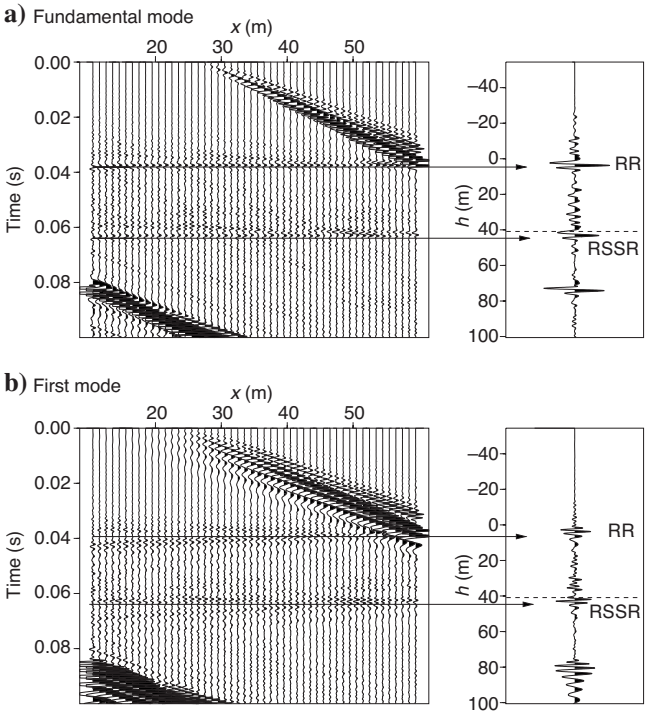

Figure 14. Deconvolution and stacking of backward-propagating Rayleigh waves. (a) After deconvolution of fundamental mode dispersion ($n = m = 0$). (b) After deconvolution of first-mode dispersion ($n = m = 1$). Stacked seismograms show distance from the front face (equation 13). Horizontal dashed lines indicate "true" distance of the fault zone.

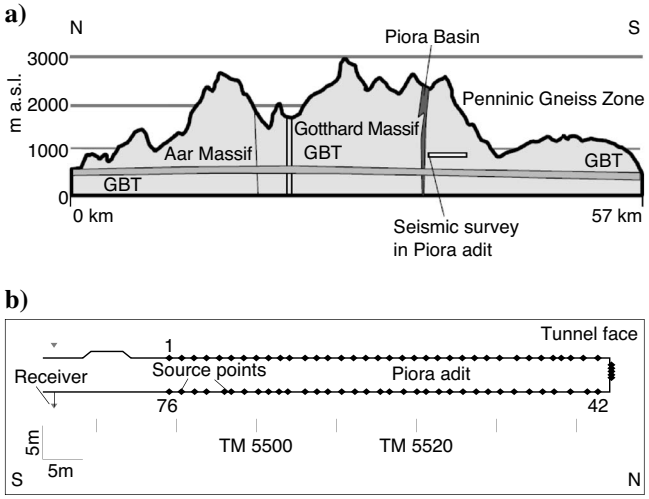

Figure 15. (a) Vertical geologic cross section along the Gotthard base tunnel. The seismic survey was performed in the Piora adit (white rectangle), which is located south of the Piora Basin. (b) Top view of the survey geometry at the tunnel face of the Piora adit. Receiver locations are indicated by inverted triangles, source points by black diamonds. In this paper, the data corresponding to the receiver and source points 42 through 76 on the right tunnel wall were used.

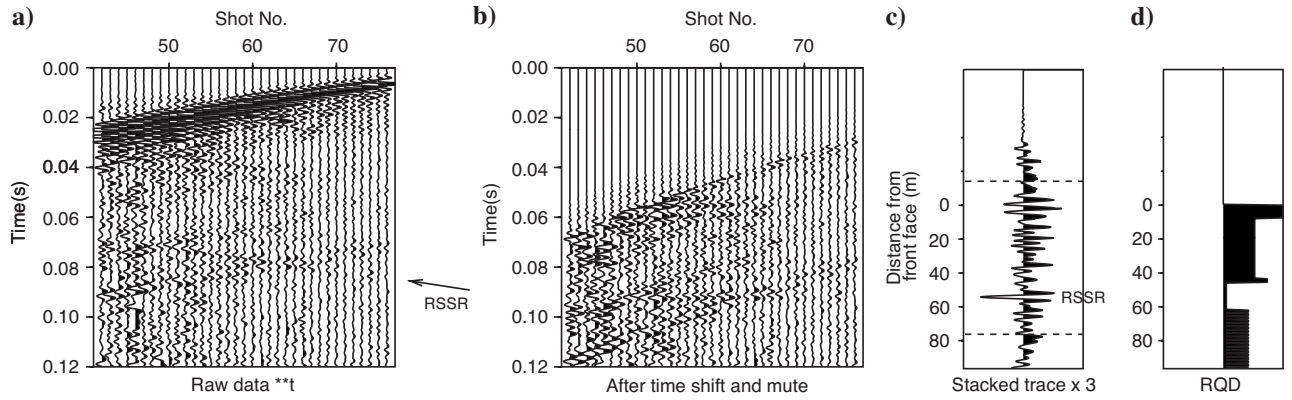

Figure 16. RSSR processing and stacking of the real data acquired in front of the Piora fault (Figure 15). (a) Common-receiver gather acquired on the right tunnel wall (Figure 15b). Amplitudes are scaled linearly with time to enhance later events. The RSSR wave is identifiable in the raw data. (b) After time shift with arrival time of direct Rayleigh wave. (c) Stack with enhanced RSSR event. The time axis was converted to distance ahead of the front face using equation 13. (d) RQD profile into the direction of drilling.

CONCLUSIONS

In this paper, we present a new and promising approach for seismic detection of structures ahead of tunnel construction that has been discovered by 3D elastic FD modeling. High-amplitude Rayleigh waves that are commonly regarded as noise in tunnel seismic exploration are utilized. Arriving at the front face, they are converted into high-amplitude S-waves propagating further ahead. Reflected or backscattered S-waves are converted back into Rayleigh waves. Finite-difference modeling suggests that these RSSR waves exhibit much higher amplitudes than body waves, if the seismic sources and receivers are located close to the tunnel wall, which can easily be recognized technically. An improved signal-to-noise ratio of this event, compared to body waves, can generally be expected in real data. Another technical advantage is that neither the sources nor the receivers need to be placed near the front head face where drilling takes place. The interference with the ongoing excavation process can thus be kept small. The excavation damage zone around the tunnel can lead to a dispersion of the Rayleigh waves. For imaging ahead, this seems to be advantageous because many different reflection responses corresponding to different combinations of transmitted and received modes can be acquired. Depending on the number of excited modes, we may obtain more reflection responses than can be achieved by conventional body wave methods. The reflection responses for different mode combinations will yield new information that may be useful for characterizing the reflectivity ahead of the construction. A repetitive application while drilling and the implementation of RSSR modes into prestack migration techniques, e.g., Kirchhoff migration, are the next steps for improving the localization of reflectors ahead of the tunnel.

We show a first observation of the RSSR wave in a field experiment that has been performed in the Gotthard base tunnel designed on the basis of the modeling results. The analysis clearly reveals that the RSSR event is generated at a prominent kakiritic zone ahead of the tunnel. Further field tests are currently being performed to explore the validity of the modeling results and the application potential of this wave type under real underground conditions.

ACKNOWLEDGMENTS

Figure 1 was provided by Birgit Schöbel (GeoForschungsZentrum Potsdam). The authors thank B. Rötlisberger and F. Walker (construction-site management, Faido tunnel) for technical support during the seismic measurements. Constructive comments by the assistant editor and anonymous reviewers helped to improve the paper. This is publication no. GEOTECH-291 of the R&D-Program GEOTECHNOLOGIEN funded by the German Ministry of Education and Research (BMBF) and the German Research Foundation (DFG), grant 03G0637B.

REFERENCES

Ashida, Y., 2001, Seismic imaging ahead of a tunnel face with three-component geophones: International Journal of Rock Mechanics and Mining Sciences, **38**, 823–831.

Bohlen, T., 2002, Parallel 3-D viscoelastic finite-difference seismic modelling: Computers and Geosciences, **28**, 887–899.

Bohlen, T., S. Kugler, G. Klein, and F. Theilen, 2004, 1.5-D inversion of lateral variation of Scholte wave dispersion: Geophysics, **69**, 330–344.

Bohlen, T., and E. Saenger, 2006, Accuracy of heterogeneous staggered-grid finite-difference modeling of Rayleigh waves: Geophysics, **71**, no. 4, T109–T115.

Borm, G., R. Giese, C. Klose, S. Mielitz, P. Otto, and T. Bohlen, 2003a, ISIS - integrated seismic imaging system for the geologic prediciton ahead in underground construction: 65th Annual Conference and Exhibition, EAGE, Extended Abstracts.

Borm, G., R. Giese, and P. Otto, 2003b, Integrated seismic imaging system for geologic prediction ahead of a tunnel construction: Presented at the 10th International Congress on Rock Mechanics.

Cerjan, C., D. Kosloff, R. Kosloff, and M. Reshef, 1985, A nonreflecting boundary condition for discrete acoustic and elastic wave equations: Geophysics, **50**, 705–708.

Deere, D. U., and D. W. Deere, 1988, The rock quality designation (RQD) index in practice, *in* L. Kirkaldie, ed., Rock classification systems for engineering purposes, American Society for Testing and Materials.

Dickmann, T., and B. Sander, 1996, Drivage concurrent tunnel seismic prediction: Felsbau-Rock and Soil Engineering, **14**, 406–411.

Dougherty, M., and R. Stephen, 1988, Seismic energy partitioning and scattering in laterally heterogeneous ocean crust: Pure and Applied Geophysics, **128**, 195–239.

Forbriger, T., 2003, Inversion of shallow-seismic wavefields: I. Wavefield transformation: Geophysical Journal International, **153**, 719–734.

Giese, R., C. Klose, and G. Borm, 2005, In situ seismic investigations of fault-zones in the Leventina Gneiss complex of the Swiss Central Alps: Geological Society Special Publication 240, 15–24.

Inazaki, T., H. Isahai, S. Kawamura, T. Kuruhashi, and H. Hayashi, 1999, Stepwise application of horizontal seismic profiling for tunnel prediction ahead of the face: The Leading Edge, **18**, 1429–1431.

Kneib, G., A. Kassel, and K. Lorenz, 2000, Automated seismic prediction ahead of the tunnel boring machine: First Break, 295–302.

Levander, A., 1988, Fourth-order finite-difference P-SV seismograms: Geophysics, **53**, 1425–1436.

Lüth, S., S. Buske, R. Giese, and A. Goertz, 2005, Fresnel volume migration of multicomponent data: Geophysics, **70**, no. 6, 121–129.

Lüth, S., R. Giese, P. Otto, K. Krüger, S. Mielitz, T. Bohlen, and T. Dickmann, 2007, Seismic investigation of the Piora Basin using S-wave conversions at the tunnel face of the Piora adit (Gotthard Base Tunnel): International Journal of Rock Mechanics and Mining Sciences, .

McMechan, G., and M. Yedlin, 1981, Analysis of dispersive waves by wave field transformation: Geophysics, **46**, 869–874.

Morse, P., and H. Feshbach, 1953, Methods of theoretical physics: McGraw-Hill Book Co.

Neil, D., K. Haramy, D. Hanson, and J. Descour, 1999, Tomography to evaluate site conditions during tunneling: 3rd National Conference of the GeoInstitute, American Society of Civil Engineers, Geotechnical Special Publication, 89, 13–17.

Petronino, L., and F. Poletto, 2002, Seismic-while-drilling by using tunnel boring machine noise: Geophysics, **67**, 1798–1809.

Robertsson, J., J. Blanch, and W. Symes, 1994, Viscoelastic finite-difference modeling: Geophysics, **59**, 1444–1456.

Schneider, T., 1997, Gotthard-Basistunnel: Neue geologische Erkenntnisse im Bereich des Tavetscher Zwischenmassivs und der Piora-Mulde. Schweizerischer Ingenieur- und Architekten-Verein, D 0143.

Schuster, K., H. Alheid, and D. Boddener, 2001, Seismic investigation of the excavation damaged zone in opalinus clay: Engineering Geology, **61**, 189–197.

Virieux, J., 1986, P-SV wave propagation in heterogeneous media: Velocity-stress finite-difference method: Geophysics, **51**, 889–901.

Wang, R., 1999, A simple orthonormalization method for stable and efficient computations of Green's functions: Bulletin of the Seismological Society of America, **89**, 733–741.